



Fabrication of thin-film batteries composed of LiCoO_2 , Li_3PO_4 , and Li layers

Tsuyoshi Ohnishi¹

Received: 31 January 2024 / Revised: 23 March 2024 / Accepted: 23 March 2024
© The Author(s) 2024

Abstract

This paper reports the fabrication of thin-film batteries which are composed of three stacking layers: LiCoO_2 , Li_3PO_4 , and Li. First, a LiCoO_2 layer is constructed on an electron-conductive substrate by pulsed laser deposition as a cathode. The crystallinity of the LiCoO_2 layer is mainly controlled by the cationic ratio of Li and Co. Subsequently, an amorphous Li_3PO_4 layer with a high ionic conductivity is further deposited on the cathode LiCoO_2 layer by radio frequency magnetron sputtering as a solid electrolyte. To avoid any possible damage which causes the formation of resistive species between LiCoO_2 and Li_3PO_4 , bias control of the substrate during Li_3PO_4 deposition is essential. Finally, a Li metal layer is deposited as an anode/current collector on the $\text{Li}_3\text{PO}_4/\text{LiCoO}_2$ bilayer by resistive heating evaporation in a vacuum at an elevated temperature for the formation of a low resistive interface. The fabricated three-layer thin-film battery shows a high-rate capability when the LiCoO_2 layer is a (104)-oriented epitaxial film.

Introduction

All solid-state Li-ion batteries are expected as next-generation batteries with their very high safety, high energy density, high power, and long cycle life. When the solid materials come into contact with each other in the battery, the interface between the materials plays a significant role in determining the battery's performance [1]. Utilization of solid-state batteries in the thin film configuration is an effective way to investigate the interfacial properties since it simplifies the geometry of the cell to extract important information from the interface by a variety of surface characterization techniques [2–5].

Thin-film batteries are already available commercially, having a relatively high power density and long cycle life with flat-shaped geometry. These features originate from the thin film shape, large reaction area per unit weight of active materials, and high electrochemical stability of the solid electrolyte. Weak points of thin-film batteries as compared to bulk ones are small capacity limited by cathode

weight and high manufacturing cost, which I am not trying to improve in this paper.

On the other hand, properties of thin film are in general different from the bulk single crystal, usually degraded due to lattice defects and therefore low crystallinity, derived from nonstoichiometry and thermal non-equilibrium. If thin films with bulk single-crystal quality are obtained, we may be able to extract the latent potential of battery materials, which bulk-shaped materials cannot access.

Here, I report the fabrication of quality-conscious thin-film batteries composed of a cathode LiCoO_2 layer grown by pulsed laser deposition, a solid electrolyte Li_3PO_4 layer deposited by radio frequency magnetron sputtering, and anode Li layer formed by resistive heating evaporation in vacuum to extract potential abilities of battery materials. The adopted preparation method of each layer is selected based on the quality first, which is described in each layer formation part.

LiCoO_2 layer growth by pulsed laser deposition

Pulsed laser deposition (PLD) is widely used to form thin films of multi-cation oxides with high- T_c superconduction, ferroelectricity, ferromagnetism, etc. in laboratories since the film formation process is simple and easy. In the PLD

✉ Tsuyoshi Ohnishi
ohnishi.tsuyoshi@nims.go.jp

¹ Research Center for Energy and Environmental Materials (GREEN), National Institute for Materials Science (NIMS), 1-1 Namiki, Tsukuba, Ibaraki 305-0044, Japan

process, fragments typically in a molecular or even atomic level are ablated from the target material if the laser photon energy is higher than its band gap, enabling the molecular level layer-by-layer growth. This was previously confirmed by the observation of intensity oscillations in reflection high-energy electron diffraction (RHEED) during epitaxial growth [6]. Furthermore, ablated single metal atom or metal oxide molecules with a different velocity and angular distribution were observed by the laser-induced fluorescence (LIF) technique [7, 8].

The laser energy density (fluence) is a very important growth parameter in PLD since it determines the composition of species ablated from the stoichiometric target [10–12]. Approximately stoichiometric fragments ($\text{Li}/\text{Co} \sim 1$, congruent ablation) can be ablated from the stoichiometric target ($\text{Li}_{1.0}\text{CoO}_2$ in the present case) only when the fluence is in the vicinity of an ablation threshold. The threshold fluence is ca. 0.20 J cm^{-2} when the KrF excimer laser is used based on the investigation of the film deposition rate [13].

P_{O_2} also becomes a critical parameter, particularly in the case of the Li compound. Because Li is the lightest metal element and is even lighter than molecular oxygen, it is often fed into the vacuum chamber to compensate for oxygen deficiency in the film during oxide thin-film growth. When P_{O_2} is increased to a level high enough to deviate from the molecular beam epitaxy (MBE) conditions, the interaction between the ablated species and oxygen molecules becomes more significant, which is observed as a decreased deposition rate. Since laser-ablated species are typically decomposed to the atomic level, lighter Li and Li oxide species are preferentially scattered by oxygen molecules, compared with heavier Co species, thus decreasing the Li content in the deposited thin film. Therefore, nearly stoichiometric films

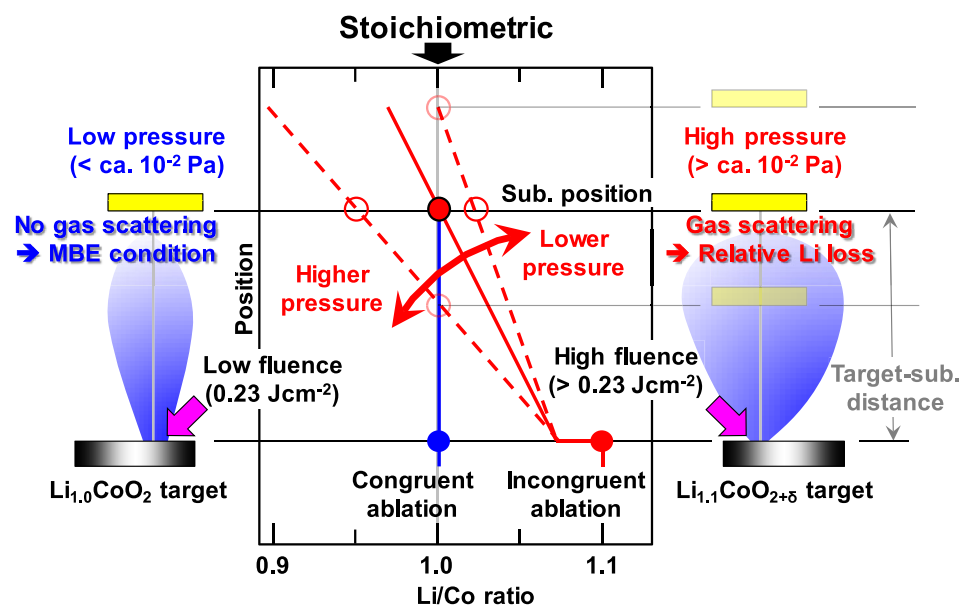
can be deposited under rather low oxygen pressure satisfying the MBE conditions where ablated species are delivered to a substrate without colliding with ambient oxygen molecules.

The resultant optimized deposition conditions are a low laser fluence of 0.23 J cm^{-2} that is barely higher than the ablation threshold for practical ablation and a low P_{O_2} of $5 \times 10^{-2} \text{ Pa}$ which is the minimum required for maintaining the oxidation state of Co^{3+} and staying within the MBE conditions [13], as illustrated in Fig. 1 left.

Although the crystallinity of the nearly stoichiometric films achieved by the optimized recipe is reasonably high, there are several operating precautions in PLD. Since the optimum fluence is in the vicinity of the ablation threshold, the deposition rate is very low; it takes more than 1 day to deposit a micrometer-thick film at a laser frequency of 10 Hz. In addition, fluctuation of laser intensity caused by the changes in room temperature brings about unstable ablation and nonuniform deposition rate. The degradation of the laser gas and/or decreased transmittance caused by the film deposition on the laser entrance viewing port may also cause the lowering of the laser intensity in particular during long-term deposition for thick-film formation. Furthermore, the decreasing transmittance is more significant under the low P_{O_2} , because the deposition of ablated species on the viewing port is further accelerated under a higher vacuum.

To overcome these problems, we examined an alternative approach, as shown in Fig. 1 right, based on the result with the stoichiometric target. First, the laser fluence is increased from 0.23 to 0.29 J cm^{-2} to increase and stabilize the deposition rate. As the fluence increases, it induces Li loss in the ablation process (incongruent ablation), resulting in the shortage of Li in the ablated species [13]. Li-enriched targets ($\text{Li}/\text{Co} > 1$) are therefore utilized to compensate for the loss.

Fig. 1 Schematic drawings of laser ablation/deposition processes (left and right) and Li/Co cation ratio variation at the plume center between target and substrate (center). Left: optimized conditions for stoichiometric $\text{Li}_{1.0}\text{CoO}_2$ target and right: examined conditions for Li-enriched $\text{Li}_{1.1}\text{CoO}_{2+\delta}$ target [9]. Copyright (2012) The Japan Society of Applied Physics



Only when the ablated species still include excess Li at the increased fluence, we can precisely tune the composition of the deposited films to stoichiometric by adjusting the P_{O_2} to scatter the excess Li by oxygen molecules.

We used a PLD system equipped with a KrF excimer laser operating at 5 Hz and capable of precise control of the “real” laser pulse energy and irradiation area on the target surface [10, 11]. The laser pulse energy used is fixed at 30 mJ, the incident angle is 45° , and the target-substrate distance is 45 mm. Sintered Li-enriched $Li_{1.1}CoO_{2+\delta}$ and $Li_{1.2}CoO_{2+\delta}$ pellets are used as targets. The substrate temperature (T_{sub}) is $800^\circ C$. P_{O_2} is optimized in the range of 5×10^{-2} – 7.5 Pa to maximize the film crystallinity from each target. Sapphire (0001) single-crystal wafers with dimensions of 10 mm square and 0.5 mm thick are used as substrates for *c*-axis-oriented epitaxy. Lattice mismatch is 2.5% when *c*-axis-oriented $LiCoO_2$ is epitaxially grown with an in-plane arrangement of $LiCoO_2$ [100] // sapphire [11 $\bar{2}$ 0].

Figure 2 shows the X-ray diffraction (XRD) patterns of approximately 180-nm-thick films grown from the $Li_{1.1}CoO_{2+\delta}$ target under P_{O_2} of 0.05, 0.1, and 3 Pa. The highest crystallinity was achieved at P_{O_2} of 0.1 Pa, as indicated by the rocking curve for $LiCoO_2$ 003 diffraction in Fig. 2b. When P_{O_2} was higher than 0.1 Pa, the Co_3O_4 phase

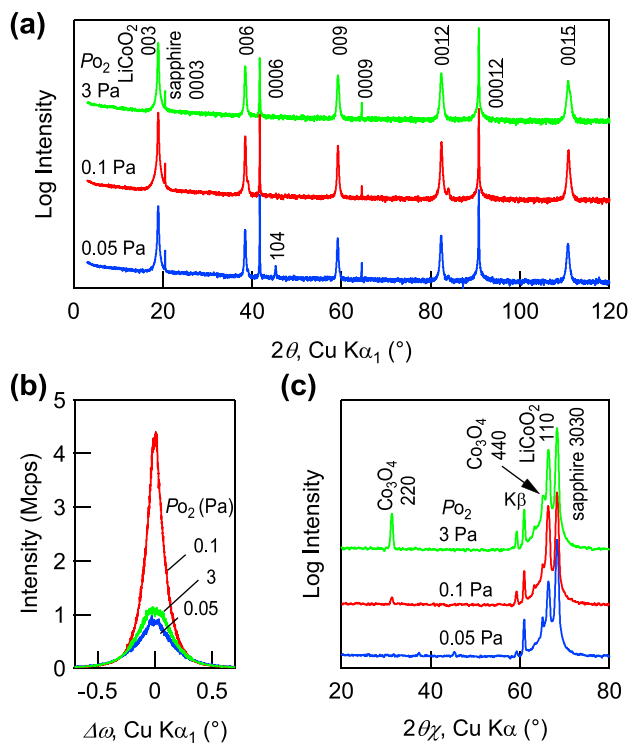


Fig. 2 XRD patterns of $LiCoO_2$ thin films grown from $Li_{1.1}CoO_{2+\delta}$ target under various P_{O_2} . **a** Out-of-plane 2θ - ω scans and **b** ω scans of $LiCoO_2$ 003 diffraction, and **c** in-plane $2\theta\chi$ - ϕ scans. Curves in **a** and **c** are offset for clarity [9]. Copyright (2012) The Japan Society of Applied Physics

was clearly observed in the in-plane diffraction pattern in Fig. 2c, which is impurity phase appeared when Li is deficient in the $LiCoO_2$ synthesis. In contrast, the Co_3O_4 phase was not detected when P_{O_2} was lower than 0.1 Pa, although the crystallinity of $LiCoO_2$ became poorer, and an unintended (104) orientation was recognized in the out-of-plane diffraction pattern.

Figure 3 summarizes the P_{O_2} dependence of (a) film thickness normalized $LiCoO_2$ 003 XRD peak intensity, (b) in-plane XRD peak intensity ratio of Co_3O_4 220 to $LiCoO_2$ 110, and (c) deposition rate per single laser pulse for the films grown by using the $Li_{1.1}CoO_{2+\delta}$ and $Li_{1.2}CoO_{2+\delta}$ targets. Data obtained for the stoichiometric $Li_{1.0}CoO_2$ target are also plotted as references [13]. Crystallinity becomes extremely high, and very little Co_3O_4 phase is found when the films were deposited from the $Li_{1.1}CoO_{2+\delta}$ target at around 0.1 Pa, as shown in Fig. 3a and b. The deposition rate of 6 pm-pulse $^{-1}$ at the P_{O_2} is ca. five times higher compared to the previous optimum condition with $Li_{1.0}CoO_2$ target. However, increasing the P_{O_2} lowers the crystallinity and increases the amount of the Co_3O_4 phase (Fig. 3b), which is considered to result from a larger amount of Li loss

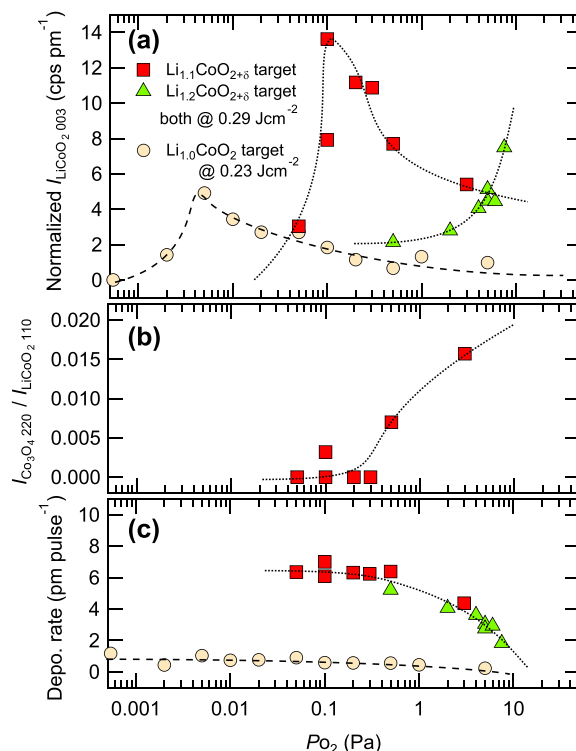


Fig. 3 P_{O_2} dependence of **a** normalized $LiCoO_2$ 003 intensity, **b** in-plane XRD peak intensity ratio of Co_3O_4 220 and $LiCoO_2$ 110 reflections, and **c** single laser pulse deposition rate. Lines are visual guides [9]. Copyright (2012) The Japan Society of Applied Physics

at higher P_{O_2} , as illustrated in Fig. 1 center. Crystallinity degradation observed at the lower side of P_{O_2} is probably due to excess Li. As a side note, the minimum required P_{O_2} to keep the oxidation state of Co^{3+} is much lower according to the results on the $Li_{1.0}CoO_2$ target [13]. We can conclude from the high crystallinity of the films obtained that cationic stoichiometry (Li/Co = 1) can be achieved at around 0.1 Pa for the $Li_{1.1}CoO_{2+\delta}$ target. The higher crystallinity compared with the films grown with the $Li_{1.0}CoO_2$ target under the optimum conditions (Fig. 3a) suggests that the films deposited from the $Li_{1.0}CoO_2$ target are still slightly Li deficient, which is due to unavoidable Li loss during the ablation process even at a low fluence of 0.23 J cm^{-2} , which is close to the ablation threshold.

When the Li content in the target further increases to $Li_{1.2}CoO_{2+\delta}$, the optimum P_{O_2} for the highest crystallinity is expected to shift to a higher pressure to scatter more Li and to make the film stoichiometric. In fact, the intensity of the 003 reflection is still increasing even at P_{O_2} of 7.5 Pa, as shown in Fig. 3a, and the maximum is considered to appear beyond the examined P_{O_2} range. However, the deposition rate dropped so severely due to the intense scattering of ablated species by ambient oxygen molecules that there is no merit to use $Li_{1.2}CoO_{2+\delta}$ or further Li-enriched targets under the current conditions when aiming at a higher deposition rate.

It should be noted here that the $Li_{1.2}CoO_{2+\delta}$ target can be used under different conditions. The clear correlation between the target composition, P_{O_2} , and the crystallinity of the obtained films strongly supports the validity of the scheme for composition control presented in Fig. 1. In this study, we varied only the P_{O_2} under a constant fluence to tune the Li/Co ratio. Figure 1 shows that, if a higher fluence was used, more Li is lost at the incongruent ablation and the optimum P_{O_2} for the desired stoichiometric deposition shifts to a lower pressure. Therefore, a relatively high deposition rate is available under the optimum P_{O_2} condition. In fact, when the fluence was varied under a constant P_{O_2} with $Li_{1.2}CoO_{2+\delta}$ targets, the intensity maximum of the 003 reflection peak appeared at a specific fluence (not shown). In addition, although the target-substrate distance was not changed in this study, it is also a controllable parameter for tuning the composition, because a longer distance will increase the loss of scattered Li. That is, the conceptual diagram in Fig. 1 predicts that the optimum conditions presented here are not the only ones, and combinations of P_{O_2} , fluence, degree of Li enrichment, and target-substrate distance, which lead to high-crystallinity stoichiometric thin-film growth under high deposition rate, are numerous [9].

Although the above results are (001)-oriented $LiCoO_2$ thin-film growth deposited on sapphire (0001) wafers, (104)-, (018)-, and (001)-oriented epitaxial $LiCoO_2$ thin films can be obtained on $SrTiO_3$ single-crystal substrates

by using (100), (110), and (111) crystal planes, respectively [14, 15]. Besides, Nb-doped $SrTiO_3$ is an electron conductor and works as a current collector in thin-film battery, although it is an *n*-type degenerated semiconductor, and the *p-n* junction resistance is added during charging when connected with $LiCoO_2$, which is a *p*-type semiconductor [16].

At the end of this chapter, the synthesis method of the $LiCoO_2$ layer is reconsidered. By using PLD, the deposition rate can be increased to a very high value if the film quality is ignored; otherwise, it is limited by requirements of the composition control, which is linked to the amount of Li enrichment in the target, allowable fluence, oxygen pressure, and so on. Furthermore, it is rather difficult to maintain the growth condition, especially the fluence, during a long-term deposition due to a degradation of laser gas and the film coating on a laser entrance viewing port, both of which reduce the laser intensity reached to the target. That is, PLD is unsuitable for thick film preparation. In connection with the film composition, PLD is also not good at preparing films with large areas. Ablation area on the target is very small (much less than 1 cm^2), and the plasma formed by ablated species (plume) is not large, several centimeters scale as illustrated in Fig. 1. Besides, usable plume portion for film deposition is restricted only to the center part (ca. 1 cm^2) since the ablated atoms or molecules have angular distribution as observed by LIF [7, 8], and the outer part is off-stoichiometric. Relatively large capacity, thick, and/or large area $LiCoO_2$ layer may be able to be prepared by chemical vapor deposition (CVD) and sputtering since the deposition rate can be stable and much higher for long-term deposition. However, CVD may not be suited since the cathode properties are sensitive to organic and other impurities left under the low growth temperature of $LiCoO_2$ (less than $1000 \text{ }^\circ\text{C}$). Indeed, sputtering is used to grow $LiCoO_2$ layers by using large targets (much larger than 1" scale) for the commercial thin-film batteries. The sputtering includes the self-adjusting mechanism of film composition, and the target composition is transferred to the film with a certain degree of accuracy. I also use sputtering to grow $LiCoO_2$ layers, which are thicker than $1 \text{ }\mu\text{m}$ [17], or as large as 45 mm diameter [18] for larger capacity thin-film batteries. Conversely, tuning of film composition by sputtering is difficult with a composition-fixed target as contrasted to fine-tunable PLD.

Li_3PO_4 layer deposition by radio frequency magnetron sputtering

Lithium phosphorus oxynitride ($LiPON$) is widely used as a solid electrolyte layer in the thin-film batteries because of its relatively high ionic conductivity ($\sim 3 \times 10^{-6} \text{ Scm}^{-1}$). $LiPON$ was first developed by Bates et al. [19] by sputtering a Li_3PO_4 target in a pure N_2 atmosphere. However,

recent first-principle calculations indicate that LiPON is not thermodynamically stable, but kinetically stabilized, upon contact with Li metal and LiCoO_2 [20]. Although partial replacement of O with N improves the ionic conductivity, incorporation of N into Li_3PO_4 narrows its electrochemical stability window according to the calculations [20].

Dopant nitrogen-free pure Li_3PO_4 is also used as a solid electrolyte layer in the thin-film batteries. Bates et al. examined it along with LiPON by sputtering Li_3PO_4 target with 40% O_2 in Ar. However, the conductivity of their Li_3PO_4 layers was as low as $7 \times 10^{-8} \text{ Scm}^{-1}$ [19], and other group also reported similar values [21], in both of which Li_3PO_4 layers were deposited by radio frequency (RF) magnetron sputtering. Meanwhile, Li_3PO_4 layers prepared by PLD using high photon energy ArF excimer laser show relatively higher ionic conductivity of $\sim 5 \times 10^{-7} \text{ Scm}^{-1}$ [22, 23], and thin-film batteries made with the PLD Li_3PO_4 operates rather nicely [23–25].

Here, I report Li_3PO_4 solid electrolyte layer synthesis by RF magnetron sputtering with much improved ionic conductivity. Although there exist difficulties in LiPON synthesis to control the incorporated amount of N and simultaneous Li addition to satisfy charge neutrality, Li_3PO_4 synthesis is much simpler. Although PLD can also prepare Li_3PO_4 layers, PLD is unsuited for thick and large-area film deposition as described earlier, to prepare thick films on multiple samples in a single deposition.

A schematic configuration of our specially designed RF magnetron sputtering system is shown in Fig. 4. Since multiple sputter cathodes with 2" diameter targets are equipped,

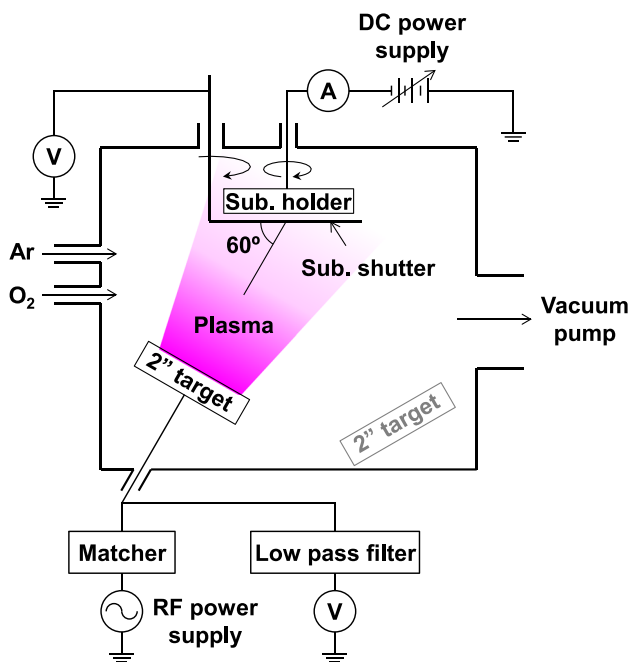


Fig. 4 Schematic configuration of a specially designed RF magnetron sputtering system [17]

each cathode is oriented to the center of a 2" diameter substrate holder with 60° incident. The substrate holder is continuously rotated during deposition, and 10 mm square or 10 mm diameter substrates are located around the middle radius position of the 2" inconel holder for simultaneous multiple deposition. Ar as well as O_2 gases can be introduced through mass flow controllers. The chamber is evacuated by a turbo molecular pump, and a conductance controllable gate valve is equipped between the chamber and pump to adjust chamber pressure independently of the gas flow rate. The substrate holder potential can be adjusted by a bipolar direct current (DC) power supply. Electron conductive substrates are used, and they are electronically connected to the substrate holder during Li_3PO_4 deposition. The sputtering plasma potential around the substrate position can be measured by a substrate shutter. Besides, the cathode DC potential can be measured through a low pass filter during RF sputtering.

It is obvious from Fig. 5 that the crystallization of the Li_3PO_4 layer drastically decreases the ionic conductivity. The figures show T_{sub} dependence of the film deposition rate, ionic conductivity, and XRD patterns of 2-h-deposited Li_3PO_4 layers on mirror-polished stainless steel substrates. The 10-mm-square and 0.5-mm-thick stainless steels, which serve as bottom electrodes, are vacuum annealed before use to remove the insulative oxidation layer on the surface. The deposition rate is evaluated by film thickness measured with X-ray reflectance measurement, and ionic conductivity is estimated by alternating-current (AC) impedance measurements with 2-mm-diameter Pt electrodes deposited by DC magnetron sputtering. The ionic conductivity is estimated from the diameter of a semi-circle at a higher frequency region by fitting. The XRD patterns are measured with the surface-sensitive grazing-incidence method (GIXRD). 150 W of RF power is used, and 200 W data are also plotted in the left panels in the figure for comparison.

The deposition rate, i.e., the resulting film thickness, is independent of the examined T_{sub} , but the T_{sub} significantly affects the ionic conductivity; the higher T_{sub} resulted in the lower conductivity. According to the GIXRD results, when T_{sub} was lower than 150°C , the Li_3PO_4 layer was an amorphous state, showing a halo centered at $2\theta = 23^\circ$. On the other hand, when T_{sub} was higher, sharp diffraction peaks appear, which correspond to the Li_3PO_4 crystal phase, and at 300°C additional peaks at $2\theta \approx 14^\circ$ and 28° appeared, which are attributable to the $\text{Li}_4\text{P}_2\text{O}_7$ crystal phase. Since the T_{sub} starting the crystallization exactly coincides with that of the conductivity dropping, it is concluded that crystallization of Li_3PO_4 impedes ionic conduction, and an amorphous state is essential for high ionic conductivity. Although low T_{sub} is preferable to make the films amorphous, the substrate is automatically heated up by sputtering plasma particularly

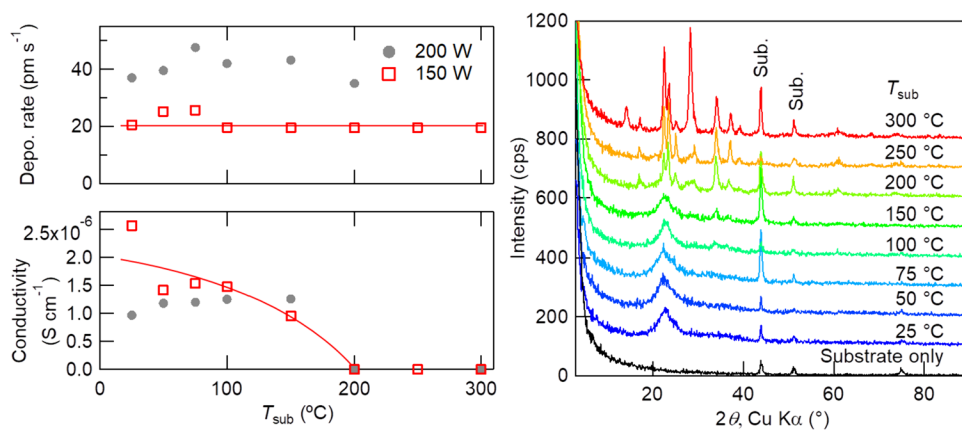


Fig. 5 Left panels: T_{sub} dependencies of the film deposition rate (top) and ionic conductivity (bottom). Lines are visual guides. Right panel: T_{sub} dependence of GIXRD patterns of 2 h-deposited Li_3PO_4 layers on stainless steel substrates with an incident angle of 0.25° . A

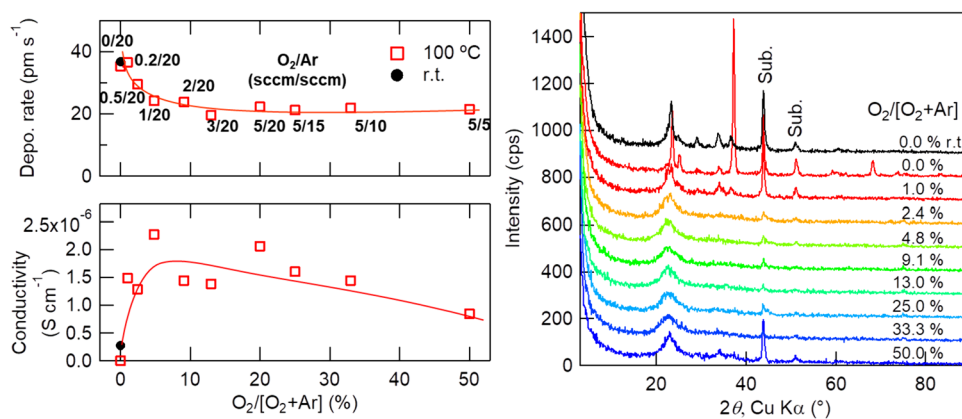
GIXRD pattern from a substrate without Li_3PO_4 deposition is also shown at the bottom. Deposition conditions are RF power 150 W, Ar 20 sccm, O_2 5 sccm, total pressure 0.6 Pa, the target-substrate distance 150 mm, and substrate bias potential +0.5 V [17]

during much longer deposition, resulting in unstable T_{sub} in our deposition system, because it does not have substrate cooler. Heating at a moderate temperature between 50 and 150 °C is reliable to keep T_{sub} constant throughout the deposition and to deposit amorphous films. Heating the substrate also helps to promote the sample degassing since it is exposed to the air before Li_3PO_4 deposition. Although the 200 W data show a higher deposition rate, almost twice, the higher cathode power tended to damage the target surface quickly and badly, e.g., cracking and color change; thus, lower RF power seems preferable for long-term deposition.

Figure 6 shows the dependence on the mixing ratio of O_2 and Ar gases, in the same manner as Fig. 5 under the total pressure of 0.6 Pa, which is controlled by the conductance valve. According to the results of Fig. 5, a T_{sub} of 100 °C is selected, and a room temperature deposition is also examined without O_2 introduction. It is obvious that the deposition rate was higher when a zero or small ratio of O_2 was introduced. However, the ionic conductivity was low, less than $10^{-6} \text{ S cm}^{-1}$ when no O_2 was introduced. GIXRD results

indicate that Li_3PO_4 was crystallized clearly when the O_2 ratio was 1% or less and slightly when it was 50%. The latter conditions seem like those examined by Bates et al. reporting low conductivity [19]; thus, it can be concluded that O_2 is necessary to avoid the crystallization; however, too much O_2 also results in the crystallization and decreases the conductivity. In addition, a thin film deposited at room temperature reveals the importance of O_2 introduction. Bragg peaks indicating crystallization were observed for the thin film deposited without O_2 introduction, even though the film was deposited without substrate heating, and the film showed low ionic conductivity. It means that O_2 gas is anyway needed to suppress the crystallization of Li_3PO_4 . Because sputtering is a vacuum process and deposited film is oxide, the film tends to become oxygen-deficient. In the field of thin-film growth of high T_c superconducting and other functional oxides, it is well-known that melting point (T_{melt}) and crystallization temperature of oxide materials tend to be lowered when oxygen is deficient, and thus, high crystallinity thin films of oxide materials with high T_{melt}

Fig. 6 Left panels: O_2 and Ar gases ratio dependences of the film deposition rate (top) and ionic conductivity (bottom). Lines are visual guides. Right panel: the same dependence of GIXRD patterns of 2-h-deposited Li_3PO_4 layers on stainless steel substrates with an incident angle of 0.25° . Deposition conditions are T_{sub} : 100 °C, RF power 150 W, total pressure 0.6 Pa, the target-substrate distance 150 mm, and substrate bias potential +0.5 V [17]



can be obtained via vacuum process [26], e.g., MBE and PLD under much lower T_{sub} relative to their T_{melt} . Besides, oxygen deficiency is introduced not only in the deposited films but also in the sputtering target, resulting in serious target damage. O_2 gas introduction is therefore necessary to suppress film crystallization and to avoid target damage in a long-term deposition for a thick solid electrolyte layer. O_2 introduction also makes the deposited films stable in air, otherwise the transparent films devitrify after long-term storage in air, probably because of the reaction with humidity.

To fabricate thin-film batteries, Li_3PO_4 layers are deposited on the above-described PLD-grown epitaxial LiCoO_2 layers. The substrates are Nb 0.5 wt%–doped SrTiO_3 (111) single crystals with 10 mm square or 10 mm diameter and 0.5 mm thick, and the composition controlled LiCoO_2 is growing in (001) orientation with a thickness of 100 to 200 nm. Figure 7 shows 2θ - ω scan XRD patterns of 15-h Li_3PO_4 -deposited (2 to 2.5 μm thick) LiCoO_2 layers under different substrate bias potentials during sputtering. Diffraction patterns before the Li_3PO_4 deposition are also shown in blue curves. It is obvious that there is a clear substrate bias potential dependence of LiCoO_2 crystallinity after Li_3PO_4 deposition. When the potential was lower than -3 V or higher than $+0.5$ V, LiCoO_2 diffraction peaks disappeared, or intensity decreased drastically; i.e., the LiCoO_2 crystal

lattice was destroyed. Besides, it seems that there is an optimal substrate potential, and -2.0 V is close to the optimal in these depositions since the intensity decrease of LiCoO_2 diffraction was minimal.

It should be noted here that the conductivity of Li_3PO_4 layers deposited on stainless steel substrates is almost constant ($\approx 1.2 \times 10^{-6} \text{ Scm}^{-1}$) in the examined potential range. This result is inconsistent with the reported results of the bias-controlled LiPON layers on liquid N_2 -cooled substrates (-80 °C) [27], where the ionic conductivity as well as Li content depends on the substrate bias. It is considered that the T_{sub} causes the difference. At a very low temperature, the deposited species sputtered from the target are quenched and solidified as they are. On the other hand, Li content in the deposited film can be self-tuned at a high temperature during the deposition since the ionic conductivity of Li_3PO_4 is significantly enhanced at a high temperature.

Here, we discuss what happens when the substrate bias potential is not optimal. Since Li_3PO_4 and LiCoO_2 do not react with each other at such a low substrate temperature as 100 °C, there must be other possible factor which relates to the potential. In a battery, the LiCoO_2 cathode can be damaged by overcharging and overdischarging, with too high and too low cutoff voltages, respectively. In the sputtering process, the DC potential of the sputtering cathode always becomes negative to sputter the target material by positively ionized Ar gases. Even though it depends on the total pressure, target-substrate distance, and on-axis/off-axis geometry [21], the target and substrate are electrically connected to each other by plasma, which is electron conductive gas; thus, the substrate holder feels the cathode potential to some extent. Since LiCoO_2 is underneath the already deposited Li_3PO_4 , which is connected to the plasma, LiCoO_2 can be charged or discharged depending on the substrate bias potential relative to the plasma potential. The LiCoO_2 film in the top of Fig. 7 seems overcharged since X-ray diffraction intensity is much decreased and additional reflections appearing at $2\theta \approx 21.6^\circ$ and 44.0° are attributable to 001 and 002 diffractions of the O1 phase, respectively, which is an overcharged phase of LiCoO_2 [28, 29]. In the figure, the bottom one seems overdischarged since LiCoO_2 cannot uptake extra Li [30], unlike $\text{LiNi}_{0.5}\text{Mn}_{1.5}\text{O}_4$ cathode [25, 31], and thus, the LiCoO_2 crystal collapses.

The shutter potential can be an appropriate reference to obtain the optimal substrate bias potential; however, it is not stable enough for long-term Li_3PO_4 sputtering, e.g., 15-h deposition; it can be shifted by changes of the target surface state: sudden target cracking, oxygen deficiency introduction, and so on. Therefore, even if the substrate bias potential once is determined from the shutter potential before the deposition, the shift of the plasma potential deviates the substrate bias potential from the optimum value during deposition, which results in low experimental reproducibility.

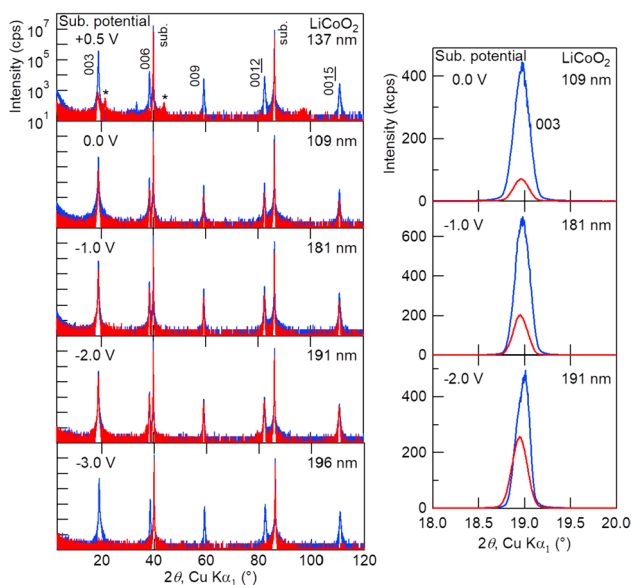


Fig. 7 Red curves: 2θ - ω scan XRD patterns of 15-h Li_3PO_4 -deposited (2 to 2.5 μm thick) LiCoO_2 thin films under different substrate bias potentials during sputtering. Deposition conditions are T_{sub} 100 °C, RF power 120 W, Ar 20 sccm, O_2 7 sccm, total pressure 0.6 Pa, and the target-substrate distance 150 mm. XRD patterns before Li_3PO_4 deposition are also shown in blue curves, and LiCoO_2 thickness is written in right top of each panel. Right panels are magnified views around LiCoO_2 003 in linear intensity scale at the substrate potentials of 0.0 V, -1.0 V, and -2.0 V. Diffraction peaks marked by “*” in the left top panel indicate O1 phase 00l [17]

Here, we introduce a strategy to solve the reproducibility problem rather easily. During Li_3PO_4 deposition, the substrate bias potential is adjusted in real time so that the current meter between the substrate holder and DC power supply (Fig. 4) shows zero current. Ideally, no current flows when the substrate bias potential and potential induced from the plasma are balanced. With this active control, we have avoided the degradation of LiCoO_2 layers by overcharging or overdischarging.

Li layer deposition by vacuum evaporation

Finally, the Li metal layer is deposited on the $\text{Li}_3\text{PO}_4/\text{LiCoO}_2$ bilayer as an anode electrode by vacuum evaporation to yield a full cell in the thin-film battery configuration. Vacuum evaporation is a simple and easy film deposition method as compared to PLD and sputtering and is valid for pure metals with low melting point/high vapor pressure, exactly like Li. Since cathode LiCoO_2 contains Li for charging, additional Li is not necessary as far as Li metal plating and striping take place during charging and discharging, respectively, in a reversible fashion, and therefore, Li-free battery should be fabricated only with electrically conductive current collector on the $\text{Li}_3\text{PO}_4/\text{LiCoO}_2$ bilayer. However, the Li-free battery does not operate properly because Li metal is extremely reactive with moisture or contaminants existing at the Li_3PO_4 surface, resulting in the formation of irreversible byproducts such as LiOH and Li_2CO_3 . Besides, Li metal plating at the interface between Li_3PO_4 and metal current corrector, e.g., Cu, needs certain energy, and therefore, it could cause additional resistance. On the other hand, once the Li metal layer is preformed, smooth Li plating takes place, and the Li consumed by the side reactions can be compensated as well.

A Li wire with a length of ca. 5 cm and a diameter of 2 mm is used as a Li source, which is evaporated from a boat made of W by resistive heating in vacuum ($\sim 5 \times 10^{-4}$ Pa), and ca. 1- μm -thick Li metal layer is deposited on the bilayers. Li deposition rate is controlled to be as high as ca. 10 nm/s by a quartz crystal microbalance throughout the deposition. It was found that the higher deposition rate brings about the higher crystallinity of the Li layer. This may be due to the avoidance of depositing impurities contained in the residual gas at a higher rate of deposition.

It is noteworthy that the bilayer samples are heated to be ca. 100 °C by Peltier heater during Li deposition, because degassing is promoted by substrate heating, and a high vacuum level can be reached in a short time. Furthermore, it is found that epitaxial Li layers with extremely high crystallinity can be obtained on sapphire wafers by substrate heating. Figure 8 indicates XRD patterns of the Li layers on sapphire wafers with different crystal planes. On sapphire a-plane

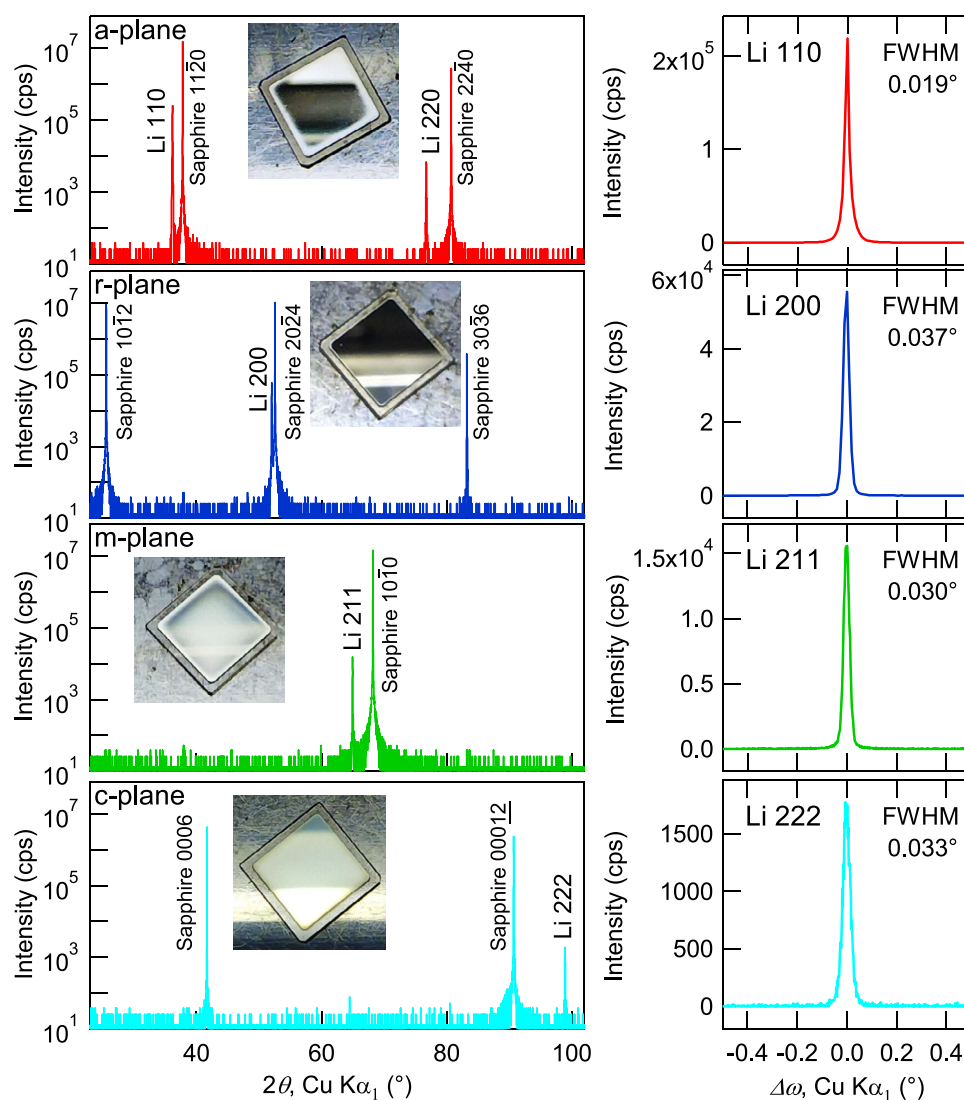
($11\bar{2}0$), r-plane ($101\bar{2}$), m-plane ($10\bar{1}0$), and c-plane (0001), Li layers are epitaxially grown in (110), (100), (211), and (111) orientations, respectively, with very narrow full width at half maximum (FWHM) of the rocking curves in ω scans. X-ray pole figure measurements confirm both out-of-plane and in-plane alignment of epitaxial Li layers. It is found that the relationship of Li (111) // sapphire (0001) and Li (100) // sapphire ($10\bar{1}2$) are fulfilled among all Li layers on the four sapphire crystal planes. It can be easily imagined that T_{melt} of Li is so low as 181 °C (456 K), and T_{sub} of 100 °C (373 K) is high enough for high crystallinity epitaxial growth of Li metal layers.

Since the Li_3PO_4 layer is amorphous, epitaxial growth of the Li layer does not take place at the $\text{Li}_3\text{PO}_4/\text{LiCoO}_2$ bilayer, and (110) orientation of the polycrystal Li layer is preferentially formed on the Li_3PO_4 . Recently, it was reported that protons infiltrated in the LiCoO_2 increase the interfacial resistance at $\text{Li}_3\text{PO}_4/\text{LiCoO}_2$ in $\text{Li}/\text{Li}_3\text{PO}_4/\text{LiCoO}_2$ thin-film batteries [32] and that the resistance can be reduced by annealing in battery form, i.e., annealing after Li layer formation [33]. Protons can be introduced into our samples from the moisture because our samples are exposed to an open air after each layer formation. One may be concerned that our thin-film batteries should have high interface resistance. However, Li layer deposition under substrate heating automatically anneals the tri-layers in battery form without a separate annealing process to reduce the interface resistance. In addition, careful degassing before and during each layer deposition by substrate heating revives a cleaner surface.

Thin-film battery

Battery performance of the fabricated $\text{Li}/\text{Li}_3\text{PO}_4/\text{LiCoO}_2$ tri-layer thin-film batteries is evaluated. Figure 9 summarizes the results of (001)- and (104)-oriented epitaxial LiCoO_2 layer batteries formed on (111) and (100) Nb:1 at%-doped SrTiO_3 ($\text{Nb}:\text{SrTiO}_3$) single-crystal substrates, as well as a preferentially (001)-oriented polycrystal LiCoO_2 layer battery made on a Au sputter-coated Si substrate. Deposition conditions of LiCoO_2 on Nb:1 at% SrTiO_3 and Au/Si substrates are the same. The samples grown on the Nb:1 at% SrTiO_3 substrates are post-annealed in air at 700 °C for 5 h to fully oxidize the LiCoO_2 films [34] and maximize the crystallinity and electrical conductance. It is confirmed that no reaction occurred between LiCoO_2 and Nb:1 at% SrTiO_3 under the annealing conditions, but it is not the case for the Au/Si substrates; thus, the post-anneal is not performed on the Au/Si sample. LiCoO_2 layer thickness is ca. 100 nm. Li_3PO_4 layer thickness is ca. 800 nm, but a three times thicker Li_3PO_4 layer is deposited on the LiCoO_2 layer on Au/Si to avoid short-circuiting because the surface of the LiCoO_2 layer on Au/Si is relatively rough.

Fig. 8 XRD patterns of ca. 1- μm -thick Li layers grown at ca. 100 °C on sapphire wafers with different crystal planes. Left: out-of-plane 2θ - ω scans and right: ω scans of the observed Li diffraction peaks. Insets in left panels are pictures of deposited Li layers. Full width at half maximum (FWHM) value of the rocking curves in ω scans is written in the right top of each right panels

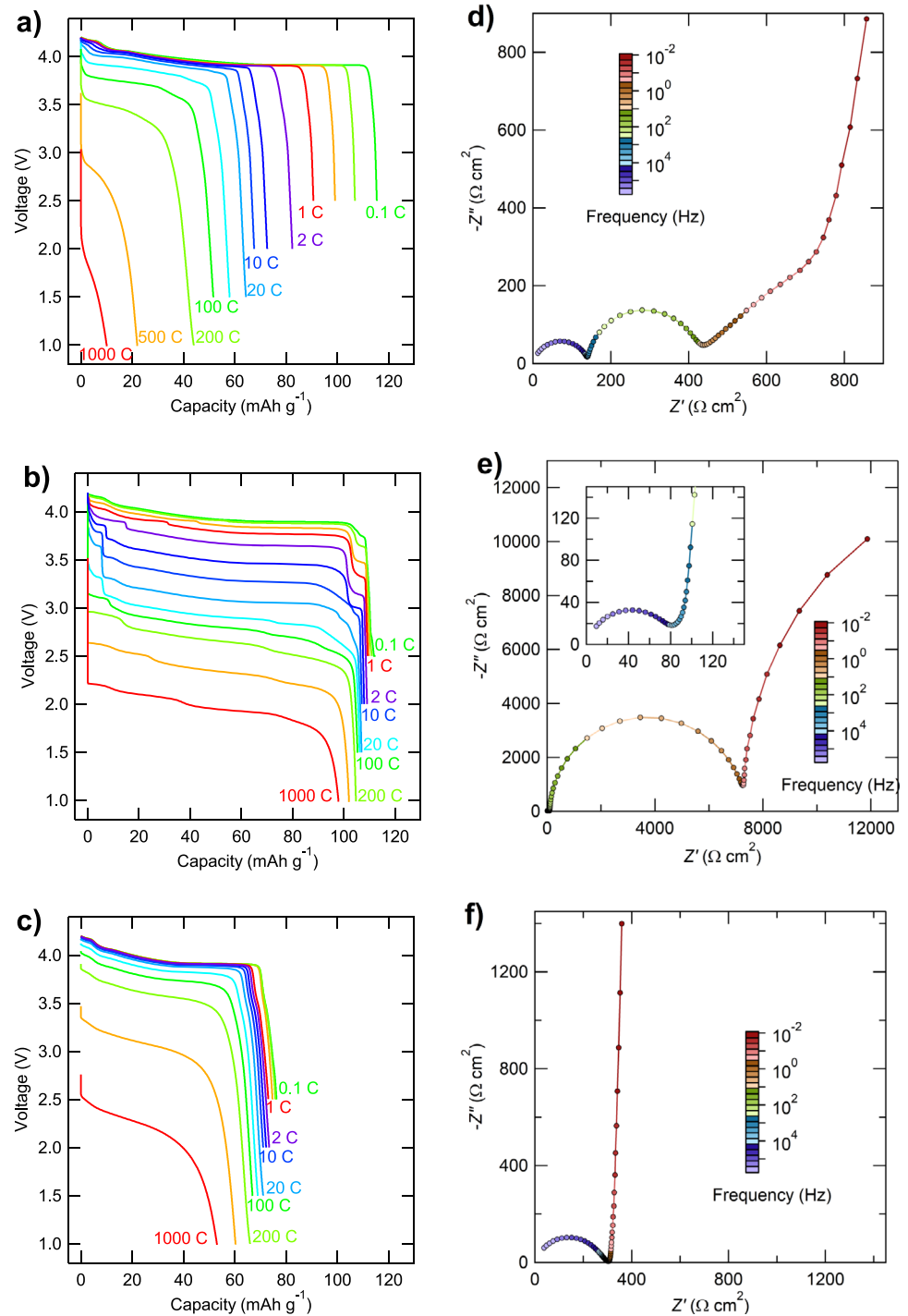


All thin-film batteries are charged at 1 C-rate constant current up to a cutoff voltage of 4.2 V, followed by constant voltage charging at 4.2 V for 2 h before each discharge. Nyquist plots of the two epitaxial LiCoO₂ layers measured by the AC impedance method at the first 4.2 V charged state (Fig. 9d and e) reveal a clear second semicircle along with a small semicircle of ca. 100 Ω cm² in the higher-frequency region. It is proved that the higher frequency semicircle originated from the ionic resistance of the Li₃PO₄ layer, as three times larger resistance is observed on the Au/Si (Fig. 9f). The second semicircles observed on the two epitaxial layer batteries are derived from the carrier-depleted space charge layer at the donor-doped SrTiO₃ side of the interface between p-type LiCoO₂ and n-type Nb:SrTiO₃. Because the discharge current flows in the forward direction in the p-n junction, the large resistance observed as the second semicircle can be ignored under high-rate discharge [16].

The two epitaxial batteries show almost the same capacity (ca. 110 mAh g⁻¹) at a low-rate discharge of 0.1 C. On the other hand, the high-rate discharge capacities are significantly different from each other; the capacity from the (104)-oriented layer at 1000 C-rate (6.05 mA cm⁻²) is 95 mAh g⁻¹, while that for the (001)-oriented is only 10 mAh g⁻¹. These results indicate that Li ion diffusion is very fast in the (104)-oriented LiCoO₂ layer but slow in the (001)-oriented layer. The results are consistent with the fact that Li-ion diffusion channels (*a-b* planes of LiCoO₂) in the (001)-oriented layer are parallel to the Li₃PO₄ layer and blocked by the CoO₂ planes, whereas the channels in the (104)-oriented layer are directly connected to the Li₃PO₄ layer, allowing facile charge transport across the cathode/electrolyte interface.

The thin-film battery on the Au/Si substrate shows a relatively higher 1000 C (5.07 mA cm⁻²) discharge capacity

Fig. 9 **a–c** Discharge curves for different C-rates and **d–f** AC impedance Nyquist plots at the first 4.2 V charged state. Cathodes are a 105-nm-thick *c*-axis-oriented epitaxial LiCoO₂ layer on 10 mm sq. Nb 1 at%:SrTiO₃ (111) (**a, d**), a 99 nm thick (104)-oriented epitaxial LiCoO₂ layer on 10 mm dia. Nb 1 at%:SrTiO₃ (100) (**b, e**), and a 94-nm-thick preferably *c*-axis-oriented polycrystalline LiCoO₂ layer on 10 mm sq. Au-coated Si (100) (**c, f**)



of more than 50 mAh g⁻¹ at the same cutoff voltage of 1.0 V, despite the smaller discharge capacity of around 80 mAh g⁻¹ at 0.1 C (507 nA cm⁻²) discharge (Fig. 9c). This relatively small discharge capacity at 0.1 C-rate is considered due to insufficient oxidation and thermal relaxation of LiCoO₂; the post-anneal is not performed on the LiCoO₂ film to avoid the anticipated reaction with the substrate. It should be noted that the LiCoO₂ layer cathode on Au/Si is

also mainly (001)-oriented, just like the LiCoO₂ on SrTiO₃ (111), which is derived from the preferential (111) orientation of the sputter-coated Au film. However, the in-plane alignment of Au and thus LiCoO₂ is random, and therefore, the LiCoO₂ cathode is polycrystalline. It contains high-density domain boundaries among the in-plane rotated LiCoO₂ (001) domains, which is different from the monolithic (001)-oriented epitaxial LiCoO₂ on SrTiO₃ (111). The

higher rate capability observed for the LiCoO₂ layer on Au/Si, despite the (001) orientation, suggests that the diffusion at the boundaries among the LiCoO₂ (001) domains is much faster [21]. The difference between Fig. 9a and c clearly indicates that the real Li-ion diffusion in the *c*-axis direction of LiCoO₂ is slow.

Conclusions

Fabrication of thin-film batteries composed of LiCoO₂, Li₃PO₄, and Li, tri-layers is described, and the correlation of the processing conditions, structure, and cell performances are discussed. The crystallinity of the cathode LiCoO₂ layer, which is directly linked to battery performance, is mainly determined by cationic composition, and Li-enriched LiCoO₂ targets are the starting point in pulsed laser deposition. The excess Li content can be controlled by oxygen pressure, laser fluence, and target-substrate distance. As for the solid electrolyte, the Li₃PO₄ layer should be amorphous for high ionic conductivity. When the Li₃PO₄ is deposited on the LiCoO₂ layer, damage control of the LiCoO₂ layer is indispensable by substrate bias tuning during sputter deposition. Finally, the anode Li layer can be formed in high quality at a high deposition rate with elevated substrate temperature. The fabricated tri-layer thin-film batteries show clear crystallographic anisotropy of LiCoO₂. The battery with the (104)-oriented LiCoO₂ cathode layer has very high-rate capability as compared to that with the (001)-oriented cathode layer.

Funding This work was partly supported by a Materials Processing Science project (“Materealize”) of the Ministry of Education, Culture, Sports, Science and Technology, Japan (MEXT); a KAKENHI Grant-in-Aid for Scientific Research on Innovative Areas “Interface IONICS” (grant number JP19H05813) from the Japan Society for the Promotion of Science (JSPS); and JST grant number JPMJPF2016.

Open Access This article is licensed under a Creative Commons Attribution 4.0 International License, which permits use, sharing, adaptation, distribution and reproduction in any medium or format, as long as you give appropriate credit to the original author(s) and the source, provide a link to the Creative Commons licence, and indicate if changes were made. The images or other third party material in this article are included in the article’s Creative Commons licence, unless indicated otherwise in a credit line to the material. If material is not included in the article’s Creative Commons licence and your intended use is not permitted by statutory regulation or exceeds the permitted use, you will need to obtain permission directly from the copyright holder. To view a copy of this licence, visit <http://creativecommons.org/licenses/by/4.0/>.

References

- Ohta N, Takada K, Zhang L, Ma R, Osada M, Sasaki T (2006) Enhancement of the high-rate capability of solid-state lithium batteries by nanoscale interfacial modification. *Adv Mater* 18:2226–1119. <https://doi.org/10.1002/adma.200502604>
- Wang B, Bates JB, Hart FX, Sales BC, Zuhr RA, Robertson JD (1996) Characterization of thin-film rechargeable lithium batteries with lithium cobalt oxide cathodes. *J Electrochem Soc* 143:3203–3213. <https://doi.org/10.1149/1.1837188>
- Iriyama Y, Nishimoto K, Yada C, Abe T, Ogumi Z, Kikuchi K (2006) Charge-transfer reaction at the lithium phosphorus oxynitride glass electrolyte/lithium manganese oxide thin-film interface and its stability on cycling. *J Electrochem Soc* 153:A821–A825. <https://doi.org/10.1149/1.2178647>
- Song J, Jacke S, Cherkashinin G, Schmid S, Dong Q, Hausbrand R, Jaegermann W (2011) Valence band offsets of LiPON/LiCoO₂ hetero-interfaces determined by X-ray photoelectron spectroscopy. *electrochem. Solid-State Lett* 14:A189–A191. <https://doi.org/10.1149/2.006112esl>
- Yamamoto K, Iriyama Y, Asaka T, Hirayama T, Fujita H, Fisher CAJ, Nonaka K, Sugita Y, Ogumi Z (2010) Dynamic visualization of the electric potential in an all-solid-state rechargeable lithium battery. *Angew. Chem. Int Ed* 49:4414–4417. <https://doi.org/10.1002/anie.200907319>
- Ohnishi T, Yamamoto T, Meguro S, Koinuma H, Lippmaa M (2007) Pulsed laser ablation and deposition of complex oxides. *J. Phys.: Conf. Series* 59:514–519. <https://doi.org/10.1088/1742-6596/59/1/111>
- Nakata Y, Kaibara H, Okada T, Maeda M (1996) Two-dimensional laser-induced fluorescence imaging of a pulsed-laser deposition process of YBa₂Cu₃O_{7-x}. *J Appl Phys* 80:2458–2466. <https://doi.org/10.1063/1.363082>
- Nakata Y, Soumagne G, Okada T, Maeda M (1998) Pulsed-laser deposition of barium titanate films and plume dynamics. *Appl Surf Sci* 127–129:650–654. [https://doi.org/10.1016/S0169-4332\(97\)00720-4](https://doi.org/10.1016/S0169-4332(97)00720-4)
- Ohnishi T, Takada K (2012) High-rate growth of high-crystallinity LiCoO₂ epitaxial thin films by pulsed laser deposition. *Appl Phys Express* 5:055502. <https://doi.org/10.1143/APEX.5.055502>
- Ohnishi T, Shibuya K, Yamamoto T, Lippmaa M (2008) Defects and transport in complex oxide thin films. *J Appl Phys* 103:103703. <https://doi.org/10.1063/1.2921972>
- Ohnishi T, Lippmaa M, Yamamoto T, Meguro S, Koinuma H (2005) Improved stoichiometry and misfit control in perovskite thin film formation at a critical fluence by pulsed laser deposition. *Appl Phys Lett* 87:241919. <https://doi.org/10.1063/1.2146069>
- Ohnishi T, Takada K (2011) Epitaxial thin-film growth of SrRuO₃, Sr₃Ru₂O₇, and Sr₂RuO₄ from a SrRuO₃ target by pulsed laser deposition. *Appl Phys Express* 4:025501. <https://doi.org/10.1143/APEX.4.025501>
- Ohnishi T, Hang BT, Xu X, Osada M, Takada K (2010) Quality control of epitaxial LiCoO₂ thin films grown by pulsed laser deposition. *J Mater Res* 25:1886–1889. <https://doi.org/10.1557/jmr.2010.0250>
- Nishio K, Ohnishi T, Akatsuka K, Takada K (2014) Crystal orientation of epitaxial LiCoO₂ films grown on SrTiO₃ substrates. *J Power Sources* 247:687–691. <https://doi.org/10.1016/j.jpowsour.2013.08.132>
- Nishio K, Ohnishi T, Akatsuka K, Takada K (2014) Corrigendum to “Crystal orientation of epitaxial LiCoO₂ films grown on SrTiO₃ substrates” [*J. Power Sources* 247 (2014) 687–691]. *J Power Sources* 261:412–413. <https://doi.org/10.1016/j.jpowsour.2014.03.067>
- Kawashima K, Ohnishi T, Takada K (2020) High-rate capability of LiCoO₂ cathodes. *ACS Appl Energy Mater* 3:11803–11810. <https://doi.org/10.1021/acsaem.0c01973>
- Ohnishi T, Takada K (2022) Sputter-deposited amorphous Li₃PO₄ solid electrolyte. *ACS Omega* 7:21199–21206. <https://doi.org/10.1021/acsomega.2c02104>

18. Kobayashi T, Ohnishi T, Osawa T, Pratt A, Tear S, Shimoda S, Baba H, Laitinen M, Sajavaara T (2022) In-operando lithium-ion transport tracking in an all-solid-state battery. *Small* 18:2204455. <https://doi.org/10.1002/sml.202204455>
19. Bates JB, Dudney NJ, Gruzalski GR, Zuhr RA, Choudhury A, Luck CF, Robertson JD (1993) Fabrication and characterization of amorphous lithium electrolyte thin films and rechargeable thin-film batteries. *J Power Sources* 43:103–110. [https://doi.org/10.1016/0378-7753\(93\)80106-Y](https://doi.org/10.1016/0378-7753(93)80106-Y)
20. Zhu Y, He X, Mo Y (2015) Origin of outstanding stability in the lithium solid electrolyte materials: insights from thermodynamic analyses based on first-principles calculations. *ACS Appl Mater Interfaces* 7:23685–23693. <https://doi.org/10.1021/acsami.5b07517>
21. Haruta M, Shiraki S, Suzuki T, Kumatani A, Ohsawa T, Takagi Y, Shimizu R, Hitosugi T (2015) Negligible “negative space-charge layer effects” at oxide-electrolyte/electrode interfaces of thin-film batteries. *Nano Lett* 15:1498–1502. <https://doi.org/10.1021/nl5035896>
22. Kuwata N, Iwagami N, Kawamura J (2009) ArF excimer laser deposition of wide-band gap solid electrolytes for thin film batteries. *J Solid State Ionics* 180:644–648. <https://doi.org/10.1016/j.ssi.2008.09.010>
23. Shiraki S, Shirasawa T, Suzuki T, Kawasoko H, Shimizu R, Hitosugi T (2018) Atomically well-ordered structure at solid electrolyte and electrode interface reduces the interfacial resistance. *ACS Appl Mater Interfaces* 10:41732–41737. <https://doi.org/10.1021/acsami.8b08926>
24. Kuwata N, Iwagami N, Tanji Y, Matsuda Y, Kawamura J (2010) Characterization of thin-film lithium batteries with stable thin-film Li_3PO_4 solid electrolytes fabricated by ArF excimer laser deposition. *J Electrochem Soc* 157:A521–A527. <https://doi.org/10.1149/1.3306339>
25. Kawasoko H, Shirasawa T, Nishio K, Shimizu R, Shiraki S, Hitosugi T (2021) Clean solid-electrolyte/electrode interfaces double the capacity of solid-state lithium batteries. *ACS Appl Mater Interfaces* 13:5861–5865. <https://doi.org/10.1021/acsami.0c21586>
26. Yun KS, Choi BD, Matsumoto Y, Song JH, Kanda N, Ito T, Kawasaki M, Koinuma H (2002) Vapor-liquid-solid tri-phase pulsed-laser epitaxy of $\text{R}\text{Ba}_2\text{Cu}_3\text{O}_{7-y}$ single-crystal films. *Appl Phys Lett* 80:61–63. <https://doi.org/10.1063/1.1432111>
27. Nakayama F, Suzuki Y, Yoshikawa K, Yamamoto S, Sakakura M, Ohnishi T, Iriyama Y (2022) Electronic properties of lithium-ion conductive amorphous lithium phosphorus oxynitride. *Chem Commun* 58:13262–13265. <https://doi.org/10.1039/d2cc05117f>
28. Amatucci GG, Tarascon JM, Klein LC (1996) CoO_2 , the end member of the Li_xCoO_2 solid solution. *J Electrochem Soc* 143:1114–1123. <https://doi.org/10.1149/1.1836594>
29. Ohnishi T, Mitsuishi K, Takada K (2021) In Situ X-ray Diffraction of LiCoO_2 in thin-film batteries under high-voltage charging. *ACS Appl Energy Mater* 4:14372–14379. <https://doi.org/10.1021/acsaem.1c03046>
30. Godshall NA, Raistrick ID, Huggins RA (1984) Relationships among electrochemical, thermodynamic, and oxygen potential quantities in lithium-transition metal-oxygen molten salt cells. *J Electrochem Soc* 131:543–549. <https://doi.org/10.1149/1.2115624>
31. Kawasoko H, Shiraki S, Suzuki T, Shimizu R, Hitosugi T (2018) Extremely low resistance of Li_3PO_4 electrolyte/ $\text{Li}(\text{Ni}_{0.5}\text{Mn}_{1.5})\text{O}_4$ electrode interfaces. *ACS Appl Mater Interfaces* 10:27498–27502. <https://doi.org/10.1021/acsami.8b08506>
32. Kobayashi S, Nishio K, Wilde M, Fukutani K, Shimizu R, Hitosugi T (2023) Protons inside the LiCoO_2 electrode largely increase electrolyte-electrode interface resistance in all-solid-state Li batteries. *J Phys Chem C* 127:4684–4688. <https://doi.org/10.1021/acs.jpcc.2c06620>
33. Kobayashi S, Arguelles EF, Shirasawa T, Kasamatsu S, Shimizu K, Nishio N, Watanabe Y, Kubota Y, Shimizu R, Watanabe S, Hitosugi T (2022) Drastic reduction of the solid electrolyte-electrode interface resistance via annealing in battery form. *ACS Appl Mater Interfaces* 14:2703–2710. <https://doi.org/10.1021/acsami.1c17945>
34. Nishio K, Ohnishi T, Osada M, Ohta N, Watanabe K, Takada K (2016) Influences of high deposition rate on LiCoO_2 epitaxial films prepared by pulsed laser deposition. *Solid State Ionics* 285:91–95. <https://doi.org/10.1016/j.ssi.2015.06.006>

Publisher's Note Springer Nature remains neutral with regard to jurisdictional claims in published maps and institutional affiliations.